Dual-Satellite Cloud Product Generation Using Temporally Updated Canonical Coordinate Features

Amanda K. Falcone, Mahmood R. Azimi-Sadjadi, *Senior Member, IEEE*, and J. Adam Kankiewicz

***Abstract*—State-of-the-art cloud products are typically generated using scientific polar orbiting satellites such as the Moderate Resolution Imaging Spectroradiometer (MODIS). However, they do not allow for observation of the same region at a regular temporal frequency, rendering them ineffectual for nowcasting problems. Operational satellites such as Meteosat-8 SEVIRI, in contrast, are geostationary and provide continual data at a regular temporal frequency over a much larger region. MODIS-like cloud products cannot be directly generated from operational satellites as they typically have a smaller number of spectral bands and different wavelengths and spatial resolution. This paper applies the canonical coordinate decomposition method to estimate scientific cloud products using imagery from operational satellites. Using the proposed method features of the Meteosat-8 imagery data that are maximally coherent with the data from the MODIS are generated. These features are temporally updated at times and locations where MODIS data are unavailable using the alternating block power method. A subset of the canonical coordinates of Meteosat-8 SEVIRI is then used to create MODIS-like cloud products using several neural networks. The quality of the generated cloud products and their temporal consistency have been demonstrated on several data sets from July 2004. A benchmarking with an independent Meteosat-8-based algorithm is also provided, which shows the promise of our approach in generating MODIS-like cloud products.**

***Index Terms*—Backpropagation neural networks (BPNNs), canonical correlation analysis, cloud mask and phase, power methods, remote sensing, temporal updating.**

I. Introduction

SATELLITE instruments provide global and local views of the Earth and atmosphere continuously, resulting in valuable but intractably large amounts of data for analysis. Many studies have been conducted on the use of statistical methods and neural networks to perform automatic classification and analysis of this large volume of data. A good overview of these efforts is found in [1]. Central to all of these nonparametric (i.e., not depend on the physical models) classification methods is the need for a human expert to create labels. This labeling process occurs on a global scale, which causes many incorrect labels on individual pixels. This lack of correctly labeled training data, in turn, leads to inaccurate automatic classification systems. In addition, for cloud classification, the traditional expert-generated labels, e.g., cirrus, cumulus, etc., are only informative about the altitude of the clouds and do not directly define their physical characteristics or compositions.

Various feature extraction methods have been examined for cloud classification problems. The use of spectral information, which is comprised of a set of radiance measurements in different spectral bands, is utilized in many cases [2]–[4]. Textural features, which are typically less sensitive to atmospheric attenuation and detector noise, are also examined [5], [6]. Some classification schemes incorporate a combination of both spectral and textural features [7]. Others [8] even account for temporal changes in the satellite data by adjusting the parameters of the classifiers to account for such changes. Temporal changes in cloud features have been further studied in [9] using a simple pixel-based approach that updates the parameters of the classifiers similar to the approach in [8].

Alternative statistical-based methods for extracting features in remote-sensing data include principal component analysis [10]–[12], independent component analysis [13]–[15], and canonical coordinate decomposition (CCD) [16]–[21]. Niemeyer *et al.* [21] utilized these algorithms to detect changes in land features using Landsat Thematic Mapper (TM) satellite data. Although these methods are used in various remote-sensing applications, their application to cloud classification has not been widely examined to date. In this paper, the application of CCD for relating two sets of satellite imagery data, namely the Moderate Resolution Imaging Spectroradiometer (MODIS) and Meteosat-8 SEVIRI, is explored.

The MODIS instrument provides data in 36 distinct spectral bands, providing a complete global coverage every one to two days [22]. The channels are processed in various combinations using meteorological algorithms [23], [24] to yield cloud products, including the cloud mask and the cloud phase that are regarded as the state of the art by scientists and meteorologists. The MODIS cloud mask designates clear versus cloudy regions in the area covered by the MODIS instrument, while the cloud phase determines the composition of the identified clouds, e.g., ice, mixed, or water phase. Due to the polar-orbiting nature of MODIS, these cloud products cannot be generated at regular temporal frequencies and over a large spatial region.

The geostationary Meteosat-8 satellite, on the other hand, provides data from the SEVIRI instrument in 11 distinct spectral bands every 15 min over a region centered on 0° longitude, covering approximately one hemisphere of the planet [25]. Owing to its increased temporal frequency and larger global

Manuscript received June 30, 2006; revised August 26, 2006. This work was supported by the Department of Defense Center for Geosciences/Atmospheric Research, Colorado State University, via Cooperative Agreement DAAD19-02-2-0005 with the Army Research Laboratory.

A. K. Falcone is with Northrop Grumman, Aurora, CO 80017 USA.

M. R. Azimi-Sadjadi is with the Department of Electrical and Computer Engineering, Colorado State University, Fort Collins, CO 80523 USA (e-mail: azimi@engr.colostate.edu).

J. A. Kankiewicz is with the Cooperative Institute for Research in the Atmosphere (CIRA), Colorado State University, Fort Collins, CO 80523 USA.

Color versions of one or more of the figures in this paper are available online at http://ieeexplore.ieee.org.

Digital Object Identifier 10.1109/TGRS.2006.888855

coverage over the MODIS, it is highly desirable to produce MODIS-like cloud products from Meteosat-8 data. However, simply applying the MODIS product algorithms to information gathered from Meteosat-8 is irrealizable due to the variation in the number of spectral bands and the auxiliary information required for cloud mask and cloud phase product generation. Although there are unpublished results using only Meteosat-8 SEVIRI imagery to produce cloud mask/phase products, as far as we know, no attempt has been made to optimally relate dual-satellite imagery data in order to create MODIS-like cloud products using the Meteosat-8 data alone without utilizing the physical models and auxiliary information typically needed to generate these products.

The motivations behind this paper are twofold. First, provide a method of classifying clouds in a manner that holds a more meaningful interpretation to cloud composition without the intervention of a human expert. The goal here is to generate MODIS-like cloud products using Meteosat-8 SEVIRI data by extracting features of Meteosat-8 that are highly coherent with the MODIS data. The second motivation is to extract a reduced set of Meteosat-8 features that are highly representative of those of MODIS and, at the same time, remove the effects of noise and uncommon (incoherent) features that could be detrimental to the classification. The CCD method provides an ideal framework for achieving these goals and, hence, is applied in this paper. In addition, the alternating block power method is used to update the canonical coordinate (CC) mappings of Meteosat-8 with each new satellite overpass when no MODIS data are available. This allows MODIS-like cloud product generation at times and locations when MODIS is not available. A subset of the CCs of Meteosat-8 is then be used to create MODIS-like cloud products using a bank of backpropagation neural networks (BPNNs). Test results and benchmarking with an independent Meteosat-8 based algorithm [26], [27] reveal the usefulness of the generated MODIS-like cloud products using only Meteosat-8 data at times and spatial locations when MODIS is not available.

The organization of this paper is as follows. A brief review of CCD and a description of the use of CCs of Meteosat-8 for features are found in Section II. The method of updating these coordinates with each new Meteosat-8 observation is found in Section III. A description of the scheme used to generate the cloud mask products using the temporally updated CC features of Meteosat-8 is found in Section IV. The cloud mask is used to generate the cloud phase product, which is found in Section V. The benchmark and validation results against a state-of-the-art Meteosat-second-generation method are discussed in Section VI. In Section VI, a comprehensive study is carried out to assess the performance of the proposed method in comparison with an independent Meteosat-8 based cloud mask and phase generation algorithm. Finally, observations and conclusions on this work can be found in Section VII.

II. CCs as Features

CCD is a method that determines linear dependence (or coherence) between two data channels by mapping the data to their CCs where linear dependence is easily measured by the corresponding canonical correlations. CCD has recently been researched for various remote-sensing problems. Okumura *et al.* [16] used CCD for noise reduction in lidar data, while Hernandez-Baquero and Schott [17] used a form of CCD to create estimates of land surface temperature from satellite data to within 1 K. Lui *et al.* [18] used CCD to determine land use, rather than surface temperature, from remotely sensed data. Studies have also been performed to show the potential of CCD for determining changes in snow cover using passive microwave data [19] and for detecting changes at nuclear power plants [20], [21].

In this paper, the CCD is applied differently than those in [16]–[21]. In that, using the two-channel CCD mapping matrices, a subset of representative Meteosat-8 features that is most coherent with those of MODIS is extracted. This subset captures most of the attributes of the MODIS data to allow for reliable MODIS-like cloud product generation when and where MODIS data are unavailable. This is accomplished without making use of any model-based lookup table matching typically used in most of cloud product generation systems. In order to understand the methodology utilized to apply CCD to the two-channel MODIS and Meteosat-8 data, first the principle behind CCD and linear dependence (coherence) is briefly reviewed [28].

A. Brief Review of CCD

Consider the composite data vector $\mathbf{z}$ consisting of two random vectors $\mathbf{x} \in \mathbb{R}^m$ and $\mathbf{y} \in \mathbb{R}^n$, $m \leq n$, i.e.,

$$\mathbf{z} = \begin{bmatrix} \mathbf{x} \\ \mathbf{y} \end{bmatrix} \in \mathbb{R}^{(m+n)}. \tag{1}$$

We assume that $\mathbf{x}$ and $\mathbf{y}$ have zero means and share the composite covariance matrix

$$R_{zz} = E[\mathbf{z}\mathbf{z}^T] = E\left[\begin{pmatrix} \mathbf{x} \\ \mathbf{y} \end{pmatrix} (\mathbf{x}^T \ \mathbf{y}^T)\right] = \begin{bmatrix} R_{xx} & R_{xy} \\ R_{yx} & R_{yy} \end{bmatrix}. \tag{2}$$

This composite covariance matrix may be taken to block tridiagonal form as follows [28]:

$$\begin{bmatrix} F^T & \mathbf{0} \\ \mathbf{0} & G^T \end{bmatrix} \begin{bmatrix} R_{xx}^{-1/2} & \mathbf{0} \\ \mathbf{0} & R_{yy}^{-1/2} \end{bmatrix} R_{zz} \times \begin{bmatrix} R_{xx}^{-T/2} & \mathbf{0} \\ \mathbf{0} & R_{yy}^{-T/2} \end{bmatrix} \begin{bmatrix} F & \mathbf{0} \\ \mathbf{0} & G \end{bmatrix} = \begin{bmatrix} I & \mathbf{\Sigma} \\ \mathbf{\Sigma}^T & I \end{bmatrix}. \tag{3}$$

The trick is to choose F, Σ, and G to be the singular value decomposition (SVD) of the coherence matrix $C = E[(R_{xx}^{-1/2}\mathbf{x})(R_{yy}^{-1/2}\mathbf{y})^T] = R_{xx}^{-1/2} R_{xy} R_{yy}^{-T/2}$. That is

$$\begin{aligned} C &= R_{xx}^{-1/2} R_{xy} R_{yy}^{-T/2} = F \Sigma G^T \\ F^T C G &= F^T R_{xx}^{-1/2} R_{xy} R_{yy}^{-T/2} G = \Sigma \end{aligned} \tag{4}$$

where $F \in \mathbb{R}^{m \times m}$ and $G \in \mathbb{R}^{n \times n}$ are orthogonal matrices, i.e., $F^T F = F F^T = I(m)$, $G^T G = G G^T = I(n)$, and $\Sigma = [\Sigma(m) \ \mathbf{0}] \in \mathbb{R}^{m \times n}$ is a diagonal singular value matrix, with $\mathbf{\Sigma}(m) = \mathrm{diag}[\sigma_1, \sigma_2, \ldots, \sigma_m]$ and $1 \geq \sigma_1 \geq \sigma_2 \geq \cdots \geq \sigma_m > 0$.

Now, the transformation

$$\begin{bmatrix} \mathbf{u} \\ \mathbf{v} \end{bmatrix} = \begin{bmatrix} F^T & \mathbf{0} \\ \mathbf{0} & G^T \end{bmatrix} \begin{bmatrix} R_{xx}^{-1/2} & \mathbf{0} \\ \mathbf{0} & R_{yy}^{-1/2} \end{bmatrix} \begin{bmatrix} \mathbf{x} \\ \mathbf{y} \end{bmatrix} \tag{5}$$

resolves $\mathbf{z}^T = [\mathbf{x}^T, \mathbf{y}^T]$ into their CCs $\mathbf{w}^T = [\mathbf{u}^T, \mathbf{v}^T]$, with the composite covariance matrix

$$R_{ww} = E[\mathbf{w}\mathbf{w}^T] = \begin{bmatrix} (R_{uu} = I) & (R_{uv} = \Sigma) \\ (R_{vu} = \Sigma^T) & (R_{vv} = I) \end{bmatrix}. \tag{6}$$

We refer to the elements of $\mathbf{u} = [u_i]_{i=1}^m \in \mathbb{R}^m$ and $\mathbf{v} = [v_i]_{i=1}^n \in \mathbb{R}^n$ as the CCs of $\mathbf{x}$ and $\mathbf{y}$, respectively. Clearly, the diagonal cross-correlation matrix Σ

$$\mathbf{\Sigma} = E[\mathbf{u}\mathbf{v}^T] = E\left[(\mathrm{W}^T\mathbf{x})(\mathrm{D}^T\mathbf{y})^T\right] = F^T C G \tag{7}$$

is called the canonical correlation matrix of canonical correlations σ_i, with $1 \geq \sigma_1 \geq \sigma_2 \geq \cdots \geq \sigma_m > 0$ and $\mathrm{W}^T = F^T R_{xx}^{-1/2}$ and $\mathrm{D}^T = G^T R_{yy}^{-1/2}$ are the overall CCD mapping matrices in (5). Correspondingly, $\Sigma\Sigma^T$ is the squared canonical correlation matrix of squared canonical correlations σ_i^2. Thus, the canonical correlations measure the correlations between pairs of corresponding CCs. That is, $E[u_i v_j] = \sigma_i \delta_{ij}$; $i \in [1, m]$, $j \in [1, n]$, with δ_{ij} being the Kronecker delta. An important property of canonical correlations is that they are invariant under uncoupled nonsingular transformations of $\mathbf{x}$ and $\mathbf{y}$ [28].

In the CCD framework, one can easily determine the rate at which the $\mathbf{x}$-channel carries information about the $\mathbf{y}$-channel and vice versa or simply the mutual information between $\mathbf{x}$ and $\mathbf{y}$. According to Shannon [29], the information rate for the composite data vector $\mathbf{z} = [\mathbf{x}^T\ \mathbf{y}^T]^T$ is defined as

$$R = H_x + H_y - H_z \tag{8}$$

where H_x is the entropy of the $\mathbf{x}$ channel data, H_y is the entropy of the $\mathbf{y}$ channel data, and H_z is the shared entropy. Using Gaussian assumptions for $\mathbf{x}$, $\mathbf{y}$, and $\mathbf{z}$ and then following derivations in [28], we may rewrite the information rate as

$$R = -\frac{1}{2}\log\det\{I - \Sigma\Sigma^T\} = \frac{1}{2}\sum_{i=1}^{n}\log\frac{1}{1-\sigma_i^2}. \tag{9}$$

The ith term in this summation, i.e., $R_i = (1/2)\log(1/(1-\sigma_i^2))$, is the rate at which the ith CC of $\mathbf{y}$, i.e., v_i, brings information about the ith CC of $\mathbf{x}$, i.e., u_i. Thus, we further refer to the R_i as canonical rates. This result implies that the rate of information captured in the first l dominant CCs of the $\mathbf{x}$ and $\mathbf{y}$ channels is the sum of the corresponding canonical rates

$$\tilde{R} = \sum_{i=1}^{l}\tilde{R}_i = \frac{1}{2}\sum_{i=1}^{l}\log\frac{1}{1-\sigma_i^2}. \tag{10}$$

The information rate (10) can be used to determine the most informative subset of the CCs for features in cloud classification. This is done by increasing l until a prespecified percent of information is captured in the first l canonical correlations.

Remark 1: A conventional method of CCD, as in (5), does not offer a simple way to compute a small subset of CCs and correlations. A full SVD for the coherence matrix, along with the square-root inverses of data covariances, has to be computed, regardless of the rank reduction. This makes the conventional method computationally intractable, especially when the data channels have large dimensions. In [30], simple algorithms using a deflation process have been reported to recursively compute the CCs and correlations one by one or in groups.

B. CCD Application to MODIS and Meteosat-8 Data

Fig. 1 illustrates the structure of the entire system used to find CC features of Meteosat-8 SEVIRI. As shown in this figure, this process involves several processing steps. First, because Meteosat-8 SEVIRI and MODIS are viewing the globe from two different orbits, each has a distinct angle at which it observes the planet. The difference in observation angles of the two instruments gives rise to problems in visible spectral bands due to differences in the angles of reflected light to the satellites. To help alleviate this problem, the data from both satellite instruments in the visible bands are partially corrected (to the first-order effects) for solar zenith angle by dividing the values of the original data returns by the cosine of the angles of the sun from the zenith. Furthermore, because of the spatial and positional differences, the data in a particular pixel of MODIS will not necessarily match the data in the same pixel of Meteosat-8 SEVIRI. Therefore, the two instruments must be geolocated in terms of their reference to the Earth. Also, Meteosat-8 SEVIRI spatial resolution at equator is approximately 9 km^2/pixel as opposed to the 1-km^2/pixel resolution for MODIS data. Therefore, the MODIS data are subsampled to represent the region covered by Meteosat-8 at the same resolution. In essence, the MODIS data are reduced spatially by averaging the data over the regions covered by Meteosat-8 to result in a pixel-to-pixel matching. This may degrade the quality of the MODIS image to some degree. However, by performing this operation in reference to the Earth, the MODIS and Meteosat-8 data sets match pixelwise in terms of the content and spatial resolution. Finally, each channel of both MODIS and Meteosat-8 is mean-centered prior to the CCD process.

After these preprocessing steps are carried out in the first subsystem of Fig. 1, it is necessary to manipulate the data into a two-channel format. For the problem of relating MODIS and Meteosat-8 SEVIRI data, we assume that the MODIS data form channel $\mathbf{x} \in \mathbb{R}^m$ and the Meteosat-8 data form channel $\mathbf{y} \in \mathbb{R}^n$ in the CCD process, where m and n $(m > n)$ are the number of their spectral bands. For the Meteosat-8 SEVIRI, there are $m = 11$ spectral bands (see Table I), while for the MODIS, $n = 19$ out of 36 spectral bands (see Table II) are used. These 19 spectral images correspond to the ones used to generate the original MODIS cloud mask product. The pixels at a specific location across the MODIS spectral images form a realization of random vector $\mathbf{x}$, while the pixels at the same location across the Meteosat-8 SEVIRI spectral images form a realization of random vector $\mathbf{y}$. There are seven infrared, ten visible, and two

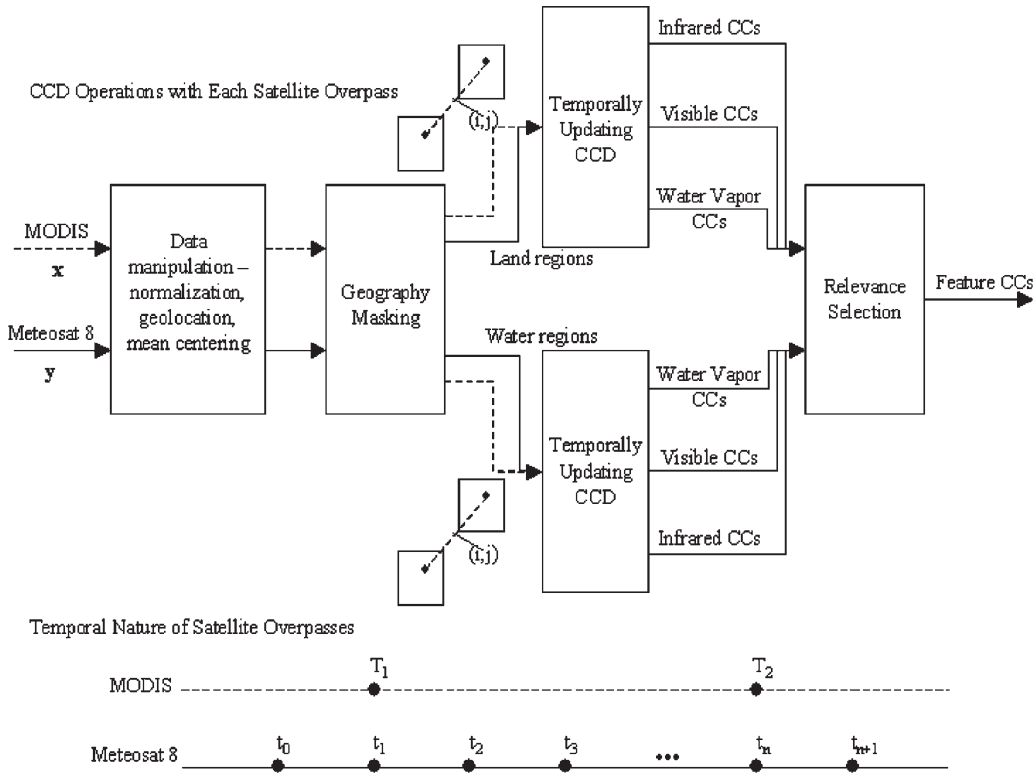

Fig. 1. Structure of the overall system used for data manipulation and CC feature extraction/selection processes.

TABLE I
SPECTRAL CHARACTERISTICS OF METEOSAT-8-SEVIRI CHANNELS

Channel Number	Channel Type	Central Wavelength (μm)	Primary use
1	Visible	0.635	Land/Cloud/Aerosol boundaries
2	Visible	0.81	Land/Cloud/Aerosol boundaries
3	Visible	1.64	Land/Cloud/Aerosol boundaries
4	Infrared	3.90	Surface/Cloud temperature
5	Water Vapor	6.25	Water vapor
6	Water Vapor	7.35	Water vapor
7	Infrared	8.70	Cloud properties
8	Infrared	9.66	Ozone
9	Infrared	10.80	Surface/Cloud temperature
10	Infrared	12.00	Surface/Cloud temperature
11	Infrared	13.40	Carbon dioxide

TABLE II
SPECTRAL CHARACTERISTICS OF MODIS CHANNELS USED IN CLOUD MASK

Channel Number	Channel Type	Central Wavelength (μm)	Primary use
1	Visible	0.645	Land/Cloud/Aerosol boundaries
2	Visible	0.858	Land/Cloud/Aerosol boundaries
4	Visible	0.555	Land/Cloud/Aerosol properties
5	Visible	1.240	Land/Cloud/Aerosol properties
6	Visible	1.640	Land/Cloud/Aerosol properties
7	Visible	2.130	Land/Cloud/Aerosol properties
17	Visible	0.905	Atmospheric water vapor
18	Visible	0.936	Atmospheric water vapor
19	Visible	0.940	Atmospheric water vapor
20	Infrared	3.750	Surface/Cloud temperature
22	Infrared	3.959	Surface/Cloud temperature
26	Visible	1.375	Cirrus clouds and water vapor
27	Water Vapor	6.715	Cirrus clouds and water vapor
28	Water Vapor	7.325	Cirrus clouds and water vapor
29	Infrared	8.550	Cloud properties
31	Infrared	11.030	Surface/Cloud temperature
32	Infrared	12.020	Surface/Cloud temperature
33	Infrared	13.335	Cloud top altitude
35	Infrared	13.935	Cloud top altitude

water vapor spectral bands of data in MODIS and six infrared, three visible, and two water vapor spectral bands in Meteosat-8 SEVIRI. Owing to the fact that the spectral characteristics of infrared, visible, and water vapor spectral bands are very different, separate sets of vectors are formed for the three different spectral regions, and the CCD process is carried out separately for these three regions. In this way, the influence of one spectral region on the CCD features of the other is avoided. Note that, although some of the spectral bands of Meteosat-8 and MODIS are similar, it is clear from Tables I and II that the MODIS data contain more information to generate much better cloud products. Clearly, our goal in the CCD process is to extract the best set of features from Meteosat-8 that is highly representative of the information in the MODIS.

After vectorizing the $\mathbf{x}$ and $\mathbf{y}$ channels, a geographical mask is applied to the samples to allow for separate CCD procedures over land and water. Again, this is based upon the knowledge that the statistics of the images over land versus over water are distinctly different. Thus, the geographical mask

separates the sample vectors into land and water areas before developing mapping matrices to create CCs of Meteosat-8. After performing this masking, a total of six sets of vectors are prepared for CCD. These vectors correspond to three different spectral regions of MODIS and Meteosat-8 imagery over land and water regions.

All the sample vectors in each set are used to create CCD mapping matrices W and D for the particular spectral band and a land or water region, as shown in the CCD subsystems in Fig. 1. Thus, the CCD processes are partitioned in the sense that a separate set of mapping matrices are developed for visible, infrared, and water vapor vectors over land and over water. By using all samples of the different vector sets, approximations to the true statistics of the data are generated.

A relevance selection procedure is then applied to determine which CC features of Meteosat-8 are to be kept and utilized in the cloud classification. This process is based solely on the information content in the CCs using the information rate in (10). The optimum number of CCs l for each spectral set over land or water is determined experimentally such that at least 70% of the mutual information between MODIS and Meteosat-8 SEVIRI is retained in the first l features. Note that this feature selection is necessary in order to ensure that only the information dominant and coherent features are used in the classification process since the subdominant coordinates tend to capture the dissimilarities (incoherence) and noise between the two satellite imagery data, which could be detrimental to classification, if included. This process also reduces the dimensionality of the feature space, which, in turn, helps to better train the classifiers. This subset of CCs of Meteosat-8 SEVIRI is subsequently applied to a classifier to create MODIS-like cloud products.

The dotted versus solid lines in Fig. 1 illustrate the fact that, while Meteosat-8 SEVIRI data are available every 15 min, the data from MODIS are only available at certain overpasses with less regularity and frequency of occurrence. The timing schedule in the lower part of Fig. 1 shows the varying overpass times of MODIS and Meteosat-8 SEVIRI. The MODIS data overpass times for the region considered here are given by T_i, where $i \in [1, M]$ is the index for the number of overpass for that particular day and M is the total number of overpasses in that day. The time between the MODIS overpasses is variable for the day, ranging anywhere between 1 and 3 h depending on the positions of the orbits of the two MODIS satellites, namely Terra and Aqua [22]. The Meteosat-8 SEVIRI data, in contrast, have overpass times designated by t_j, where $j \in [1, N]$ is the corresponding index of the overpass for the same day and N is the total number of Meteosat-8 overpasses in that day. An important distinction, however, is the fact that the Meteosat-8 overpasses occur at regular 15-min intervals. Also, each passing of the MODIS instrument over the area seen by Meteosat-8 SEVIRI results in a different area of spatial coverage. Only the areas that have overlapping data are used for computing the canonical mappings. Owing to the changes that occur over time in the satellite observations, it is obviously necessary to update the canonical mapping matrices with each new Meteosat-8 observation, even when MODIS data are not available between two overpasses. A temporal updating method is described in the next section.

III. Temporal Updating of CC Features

In order to create a temporally consistent set of features for cloud mask/phase generation, it is necessary to update the relevant CCD mapping matrices W and D with each new Meteosat-8 overpass. It was previously mentioned that the Meteosat-8 SEVIRI satellite provides data every 15 min, while the MODIS data are returned sporadically. Thus, in order to provide cloud products at times and locations where MODIS is not available, it is necessary to update the Meteosat-8 features every 15 min with new samples of the Meteosat-8 data while retaining the information of the previous MODIS as well as previous Meteosat-8 frames.

As noted before, only the first l most coherent CCs are used to classify the Meteosat-8 data into cloud products. However, as mentioned in Remark 1 in Section II-A, the conventional method of finding CCD mappings requires a full SVD of the coherence matrix C and does not allow for calculation of only a subset of the CCs. Moreover, the conventional CCD method does not allow for easy updates to the mapping matrices W and D with the arrival of new samples. The alternating block power-based method [30] provides a means of updating the several columns of these matrices as new samples of satellite data become available.

A. Temporal Updating Using Alternating Block Power Method

It can easily be shown that the problem of finding CCs can be cast as a coupled generalized eigenvalue problem, which can be solved using the alternating power method [31] by using alternating iterations. In [30], an alternating block power method was introduced, which allows solving for several columns of W and D at the same time. That is, given the prior knowledge of how many columns are needed to meet certain percentage of mutual information rate, the first l columns of the mapping matrices W and D can be computed, leading to the top l CCs of each channel. In our specific application, l is predetermined such that the corresponding canonical correlations capture at least 70% of the mutual information [see (10)] between the satellite instruments. Note that $l \leq m$, i.e., less than or equal to the smallest dimension of $\mathbf{x}$ and $\mathbf{y}$ channels.

An iterative method in [30] computes the first l columns of mapping matrices W and D, i.e., W_l and D_l using the following alternation equations:

$$\begin{cases} \text{Solve } R_{xx}\bar{\mathrm{W}}_l(k+1) = R_{xy}\mathrm{D}_l(k) & \text{for } \bar{\mathrm{W}}_l(k+1) \\ \bar{\mathrm{W}}_l(k+1) \xrightarrow{\text{GSO}} \mathrm{W}_l(k+1) & \\ \text{Solve } R_{yy}\bar{\mathrm{D}}_l(k+1) = R_{yx}\mathrm{W}_l(k+1) & \text{for } \bar{\mathrm{D}}_l(k+1) \\ \bar{\mathrm{D}}_l(k+1) \xrightarrow{\text{GSO}} \mathrm{D}_l(k+1). & \end{cases} \tag{11}$$

Note that the second and fourth equations in (11) perform the Gram–Schmidt orthogonalization (GSO) of W_l and D_l, respectively, and they guarantee the constraints $\mathrm{W}_l^T(k+1)R_{xx}\mathrm{W}_l(k+1) = I$ and $\mathrm{D}_l^T(k+1)R_{yy}\mathrm{D}_l(k+1) = I$ for every iteration k. An iterative GSO for W_l and D_l procedure is introduced in [30]. It is worthwhile to mention that, if no prior knowledge about the number of necessary CCs l is available, the order recursive alternating method in [30] can be used to

calculate the CC mappings in a sequential manner until the mutual information criterion is met.

To implement the above algorithm, updated versions of covariance and cross-covariance matrices are required. At those time instances where both data sets are available, i.e., MODIS and Meteosat-8 SEVIRI overpasses coincide, all the covariance and cross-covariance matrices R_{xx}, R_{yy}, and R_{xy} are updated; whereas in the absence of the MODIS, only the covariance matrix R_{yy} of the new Meteosat-8 data and cross-covariance R_{xy} between the new Meteosat-8 data and the previous MODIS overpass data are updated. The covariance and cross-covariance matrices are updated using

$$\begin{cases} R_{xx}(j) = \lambda R_{xx}(j-1) + \mathbf{x}(j)\mathbf{x}^T(j) \\ R_{yy}(j) = \lambda R_{yy}(j-1) + \mathbf{y}(j)\mathbf{y}^T(j) \\ R_{xy}(j) = \lambda R_{xy}(j-1) + \mathbf{x}(j)\mathbf{y}^T(j) \end{cases} \tag{12}$$

where $\lambda < 1$ is a forgetting factor. Several different values of λ were tested, and it was experimentally determined that $\lambda = 0.75$ gave the best overall results. This value provided the most optimal mechanism for weighting the recent and past information for temporal updating of the covariance matrices. Therefore, this value was selected and used throughout our experiments. The initial estimates $R_{xx}(0) = R_{yy}(0) = R_{xy}(0) = \delta^2 I$, where δ is a small quantity. This prevents the covariance matrices from becoming singular at early iterations. After each rank-one update of the covariance matrices, the alternating block power method is iterated for some number of iterations. During these iterations, the covariance matrices are kept fixed. With the next data observation, an update of the covariance matrices takes place again, and the process is repeated.

At the start of the day when both MODIS and Meteosat-8 data sets are available, the mapping matrices are calculated using the standard SVD-based method in Section II. Then, the alternating block power algorithm is implemented during the day. During this updating process, the covariance matrix for the MODIS data is held fixed until the next MODIS overpass, but the cross-covariance matrix between MODIS and Meteosat-8, as well as the covariance matrix of the Meteosat-8 data, are updated with each new Meteosat-8 SEVIRI overpass. At the time of the new MODIS overpass, all of the covariance matrices are recomputed, and the process restarts again. As mentioned before, the temporally updating process is executed for each spectral (visible, infrared, and water vapor) and geographical (land and water) regions separately, hence resulting in six updated pairs of mapping matrices W_l and D_l.

B. Temporal Consistency and Information Rate

As discussed before, it is desirable that the retained CC features capture at least 70% of the mutual information between MODIS and Meteosat-8 for subsequent cloud mask/phase generation. In order to verify that, indeed, the retained (three infrared, two visible, and one water vapor) CC features result in the retention of 70% or more of the mutual information during the course of temporal adaptation, the information rates over land and water for July 8, 2004, from 12:00 UTC to 14:00 UTC are computed and monitored in Fig. 2(a) and (b), respectively. These rates are calculated every 15 min with each new Meteosat-8 SEVIRI overpass. In these plots, the horizontal axis represents the time elapsed since the initial time at 12:00 UTC, i.e., the first time MODIS and Meteosat-8 were available. At 13:30 UTC, after 90 min of elapsed time, the new MODIS data are used in addition to the Meteosat-8 data to recalculate the covariance matrices. Nonetheless, in between these time instances, temporal updating takes place based upon every new Meteosat-8 overpass. The information rates are calculated separately over land and water for the retained three infrared, two visible, and one water vapor CCs. Fig. 2(c) and (d) indicates different regions of the Earth covered by MODIS at 120:00 UTC and 13:30 UTC overpass times, respectively.

Several interesting observations can be drawn from these results. First, notice that, in both cases, the information rate for the retained CCs features remains above 70% at all times. This implies that the classification using these updated features should provide reasonable results. Also, the information rate over time remains fairly steady until the next MODIS overpass. This is especially true over water, where the geographical features are uniform compared to land regions. This indicates that the information rate between MODIS at time 12:00 UTC and Meteosat-8 during the time period of 12:00 UTC through 13:15 UTC is fairly consistent. However, at the time 13:30 UTC when new MODIS becomes available, there is a rather substantial change in the information rate. This change is an indication of the fact that the coherence (or linear dependence) between the two data sets is different. This is most likely due to the differences in MODIS viewing angle and coverage from one overpass to the next. In this example, the MODIS overpass at 12:00 UTC shares a viewing angle that is very close to the angle of Meteosat-8. However, at 13:30 UTC, the MODIS viewing angle is distinctly different than that of Meteosat-8. In fact, at 13:30 UTC, the MODIS instrument is viewing the covered region at a very sharp angle from the zenith of the instrument, which causes a great deal of reflection. Owing to the fact that the viewing angle of the Meteosat-8 instrument is not the same, the coherence (measured by the information rate) between the instruments will change at this point. Another important reason for this change in linear dependence is that the MODIS instrument does not return data at the same geographical location over the Meteosat-8 region with each overpass [see Fig. 2(c) and (d)]. Because various land and water features have different characteristics within the overall image, this can also lead to changes in the overall coherence. For instance, in this case, the MODIS overpass at 12:00 UTC covers the Mediterranean Sea and North Atlantic Ocean as well as land regions such as Spain and Morocco. These areas are very dark and vegetated. However, the MODIS overpass at 13:30 UTC covers the South Atlantic and sub-Saharan Africa. It is likely that different regions covered by MODIS will also contribute to differences in coherence over time. Although in this case there is a small region of land covered by MODIS in both overpasses, there is no guarantee that this will happen in consecutive passes. Thus, it is necessary to do an analysis over the entire MODIS area.

The information rate plot over land in Fig. 2(a) remains fairly flat from the initial MODIS overpass at 12:00 UTC until the time just before the next MODIS overpass at 13:30 UTC, where there is a sharp drop in coherence between the Meteosat-8

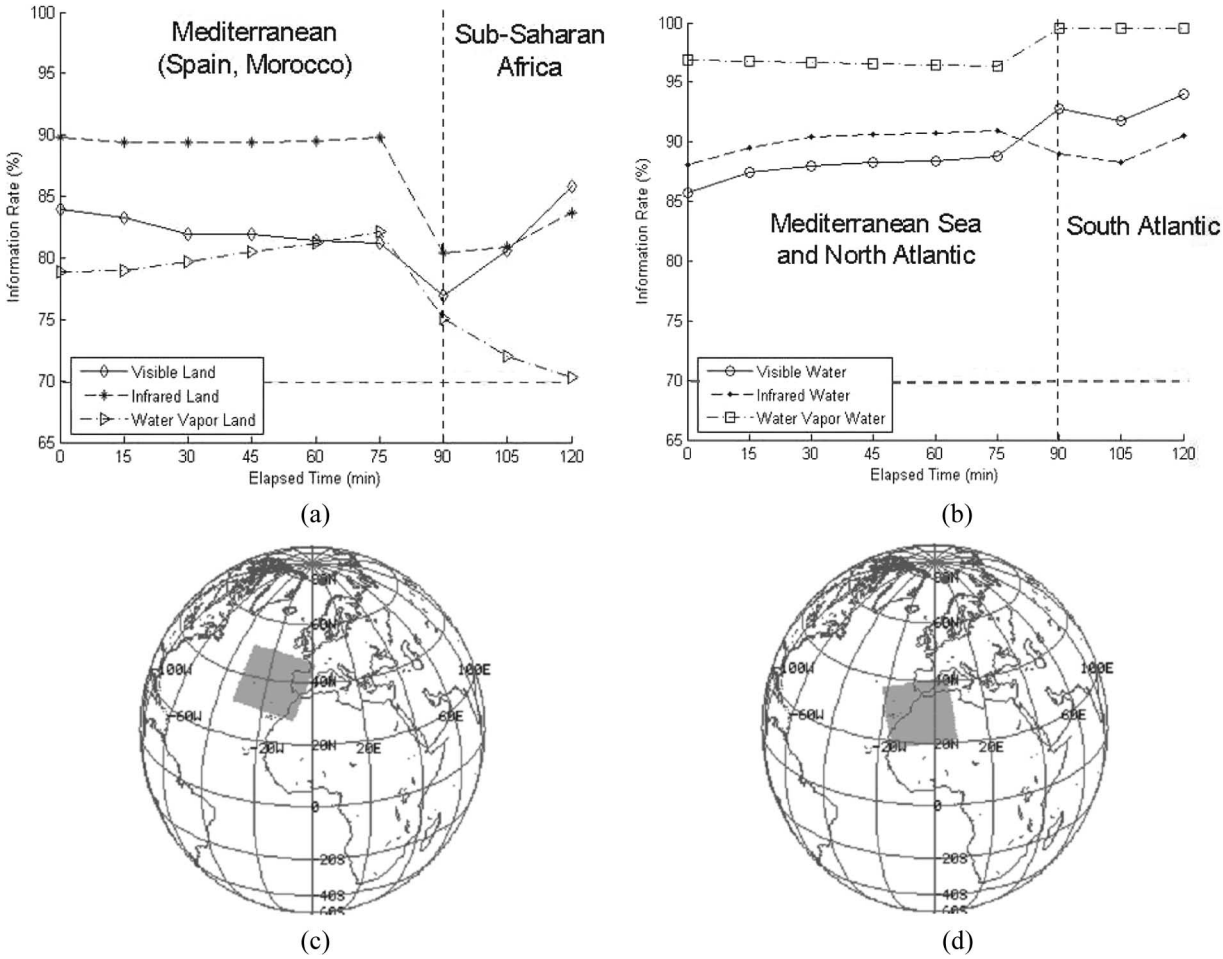

Fig. 2. Temporally updated information rates for canonical coordinates of Meteosat-8—July 8, 2004. (a) Over land. (b) Over water. (c) Map of the region covered by MODIS overpass on July 8, 2004, at 12:00 UTC. (d) Map of the region covered by MODIS overpass on July 8, 2004, at 13:30 UTC.

and MODIS data in all spectral bands. It is interesting to note that, after this MODIS overpass, the coherence between the instruments rises as a result of the temporal updating to some degree for the visible and infrared channels, while dropping for the water vapor channels. This is likely due to the rapid development of cumulus clouds in the Meteosat-8 images over time, which causes artifacts in the water vapor channels that were not available at the 13:30 UTC MODIS overpass at which the covariance matrices were updated. That is, these clouds are seen in the water vapor images of the Meteosat-8 instrument but not in the MODIS data, hence causing discrepancies in the information content. However, it is important to note that, at all times, the present information rate remains above the desired level of 70%.

The information rate plot over water in Fig. 2(b) exhibits fewer changes than those over land. The information rates remain steady throughout the 2-h span tested. This is likely due to the fact that the ocean areas do not change in temperature and reflectivity over time as dramatically as the land areas. Consequently, the new MODIS overpass data do not change the covariance matrices drastically, hence resulting in very steady information rates. The information rates for the first 90 min are very steady. A small jump in information rate occurs at the next MODIS overpass at 13:30 UTC for water vapor and visible channels, while a slight decline in information rate occurs at this point for the infrared channels. However, these changes are minor, and the rates remain steady after the MODIS overpass, indicating that there is a high coherence between the two satellite data at different times. Again, all of these rates are above the 70% desired level. Thus, the use of the three infrared, two visible, and one water vapor CCs of Meteosat-8 that retain 70% or more of the mutual information is verified experimentally.

To verify the validity of the aforementioned observations and conclusions, the information rate is calculated on an alternate day, July 7, 2004. The plots of these results over land and over water are found in Fig. 3(a) and (b), respectively. In the plot of information rate over land in Fig. 3(a), the three MODIS overpasses occur at 0 min (corresponding to 9:45 UTC), 195 min (corresponding to 13:00 UTC), and 285 min elapsed time (corresponding to 14:30 UTC). From this plot, it is obvious that, over time, the information rate over the desert region in sub-Saharan Africa remains reasonably steady for the infrared and water vapor spectral bands. There is a significant rise of coherence in the visible channels over the sub-Saharan Africa region in this period. This rise in coherence is likely due to the fact that the region seen by MODIS at 9:45 UTC is seen at a distinct angle from that seen by Meteosat-8 SEVIRI. Because of the sharpness of this angle from the MODIS zenith, the MODIS instrument is receiving more directly reflected light at this time than the Meteosat-8 instrument. However, as the day

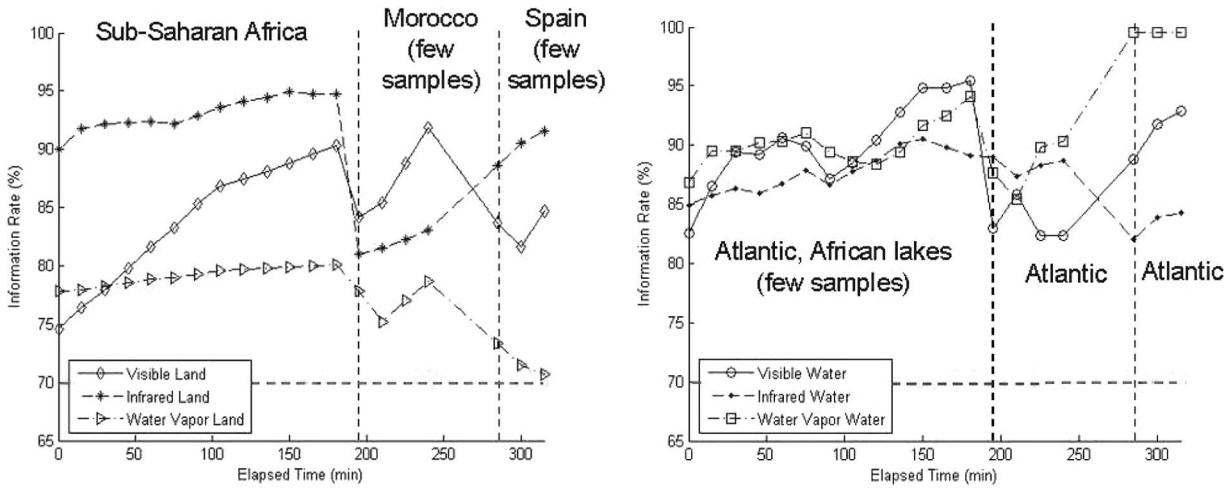

Fig. 3. Temporally updated information rates for canonical coordinates of Meteosat-8—July 7, 2004. (a) Over land. (b) Over water.

continues, the Meteosat-8 instrument receives more reflected light, which causes the coherence in the visible channels to increase. Because the water vapor and infrared channels do not depend directly on the reflected light, this change is not as dramatic in these channels. At the next MODIS overpass at 195-min elapsed time, there is a drop in the coherence in all of the spectral bands. This is likely due to the fact that there are few samples to change the MODIS covariance matrix, and thus, the changes in the data are not properly reflected over land. This is also the case at the final MODIS overpass of the day at 285-min elapsed time. However, in all cases, the coherence remains above 70%.

Similarly, Fig. 3(b) shows the changes in the information rate over water for the duration given. Notice that, for the initial duration from the first MODIS overpass until the second, there are some erratic changes in the information rate as time elapses. This is likely due to the fact that there are very few MODIS samples of the water regions with which to initialize the covariance matrices. Therefore, the initial MODIS covariance matrices over water are not necessarily accurate estimates of the true values, hence leading to discrepancies in the coherence between MODIS and Meteosat-8. However, notice that, at the second MODIS overpass at 195-min elapsed time, the information rate levels off to some degree and remains fairly steady until the next MODIS overpass. Although there are few sample points between these MODIS overpasses, the information rate steadies in this period, indicating that the linear dependence between MODIS and Meteosat-8 is reasonably consistent in this time frame. At the third MODIS overpass at 285-min elapsed time, there is a large jump in information rate for visible and water vapor wavelengths. The coherence values remain steady after this jump. At the 285-min overpass, there is a drop in the information rate in the infrared bands, but after this drop, the coherence remains reasonably steady. The changes in information rate are likely due to the changes in satellite viewing angle. Although correcting for solar zenith angle aids in the problems associated with different viewing angles, it is clearly illustrated through these plots that the differences in angle have not been completely compensated for. Part of this problem is with the amount of light returned to the various satellites that is related to the area covered by MODIS in each subsequent overpass. Because the area covered by MODIS changes, the angle of observation changes with each overpass, while the Meteosat-8 angle remains constant. Thus, there are obviously problems involved with the overpass location that cannot be solved by simply dividing by the solar zenith angle. However, the information rate is always about 70%, which again indicates that these coordinates are good features for classification.

IV. Cloud Mask Generation Process

The MODIS cloud mask algorithm uses 19 out of the 36 spectral bands from MODIS. These bands are screened and tested for cloud coverage. For each spectral test, a probability of clarity is assigned. After the various tests are performed, the results of these tests are combined to classify the pixel as one of the four possible classes that are confident clear, probably clear, uncertain, and cloudy. Typically, approximately 90% of the pixels are either classified as clear or cloudy [23]. For this experiment, classification is performed to place the Meteosat-8 SEVIRI CCs into either clear or cloudy classes, and no provision is made for the less certain clarity levels as they are ambiguous classes and cause inaccuracy in classification.

To show the usefulness of the extracted CC features for creating MODIS-like cloud masks, several BPNNs are trained based on the CC features of Meteosat-8 at different geographical regions, namely land and water, and for every 2-h span throughout the daytime. Thus, for an 8-h period during 10:00 A.M. and 12:00 P.M., four pairs of BPNNs are trained for their specific spatial locations, e.g., for regions over land and water. Note that this grouping of BPNN classifiers had to be done since it is impossible to successfully train one network to account for the spatial (over land and water) and temporal variability in the satellite data.

The input signal to each three-layer BPNN is a 6-D feature vector consisting of the CCs (three infrared, two visible, and one water vapor CCs) of Meteosat-8 for a particular pixel. Each

network has 12 neurons in the first hidden layer, six neurons in the second hidden layer, and two outputs corresponding to clear or cloudy classes. The nonlinear activation function utilized at each level is a hyperbolic tangent [32]. With this activation function, values outside of the range of $[-1, 1]$ will be mapped to a value between $[-1, 1]$. A hard-limiting threshold operation is experimentally determined to yield the best results at the output layer neuron and is used to convert the output of the network to one of the possible cloud mask levels. All of the networks are trained on 7500 randomly selected samples of the two classes for a total of 75 epochs. A rather large training data set is created by matching MODIS and Meteosat-8 SEVIRI overpasses from the week of July 7, 2004, through to July 15, 2004. The BPNNs are trained solely based on pixels labeled as confident clear or cloudy in the original MODIS cloud masks. A total of 25 different weight initializations are tried for each network, and an average classification rate of 94%–97% is found on the training data for these networks. The best networks are then selected based on the performance on the training data.

The networks are then tested on the temporally updated CC features of Meteosat-8 data. Depending on the particular time of the Meteosat-8 overpass, an appropriate pair of BPNNs is used. Classification results of these temporally updated features for July 8, 2004, are shown in Fig. 4(a)–(f). Fig. 4(a) is the original MODIS mask for only cloud and clear pixels at 12:00 UTC (initial time), while the corresponding network-generated mask at the same UTC time is found in Fig. 4(b). The overall correct classification rate for this result is around 91.40%. The overall visual appearance of this mask is very good in comparison with the original mask in Fig. 4(a). The misclassifications are sporadic, indicating that there is no particular area in which the majority of the misclassifications occur.

In order to illustrate the quality of the temporally updated features versus the features without temporal updating, the original MODIS cloud mask at 13:30 UTC is presented in Fig. 4(c). Note that this mask covers a different region within the Meteosat-8 data [see Fig. 2(d)]. The mask produced by recomputing the mapping matrices based on new MODIS and Meteosat-8 data at this time is found in Fig. 4(d), while the network-generated cloud mask created with temporally updated Meteosat-8 CCs (without the new MODIS data at 13:30 UTC) is found in Fig. 4(e). The mask found in Fig. 4(d) is clearly a closer approximation to the original MODIS cloud mask in Fig. 4(c) than that in Fig. 4(e), especially in the upper left and lower right areas of the image. This illustrates that the inclusion of the new MODIS data at the next overpass indeed adds valuable information to the features that are not captured from the previous MODIS overpass. For comparison, the network-generated cloud mask created using the CCs of Meteosat-8 without temporal updating is found in Fig. 4(f). Comparison of the two network-generated cloud mask products in Fig. 4(e) and (f) with the original MODIS cloud mask in Fig. 4(c) reveals that the cloud mask created with temporally updated features in Fig. 4(e) has a closer correspondence to the original MODIS cloud mask than that created without temporally updated features in Fig. 4(f). This is particularly clear in the upper left and lower right regions of the image, where the mask generated

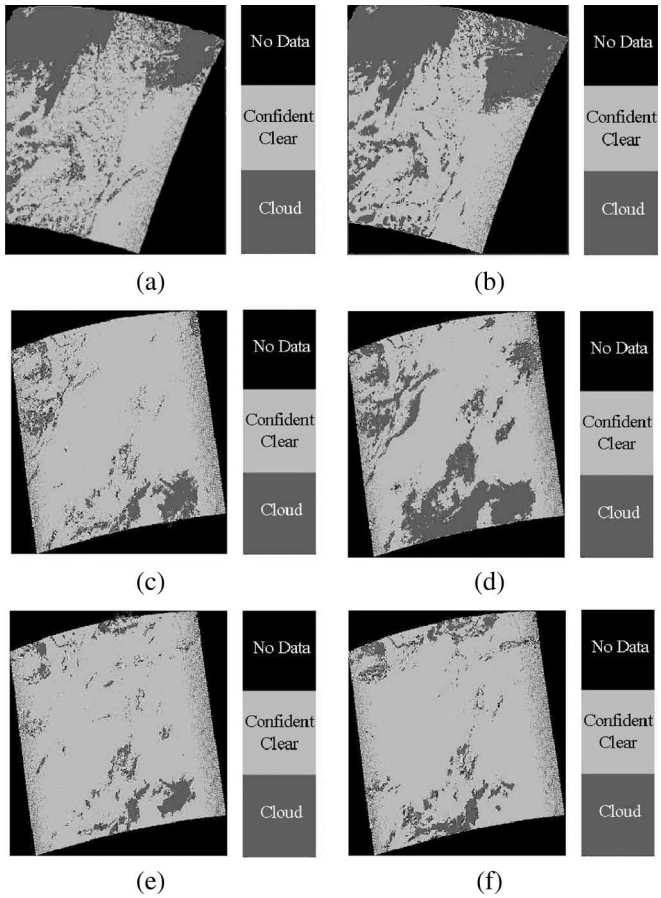

Fig. 4. MODIS cloud mask and network-generated results on July 8, 2004. (a) MODIS cloud mask at 12:00 UTC. (b) Network-generated MODIS cloud mask at 12:00 UTC. (c) MODIS cloud mask at 13:30 UTC. (d) Network-generated two-class cloud mask with retraining using both Meteosat-8 and MODIS at 13:30 UTC. (e) Network-generated two-class cloud mask with temporal updating of only Meteosat-8 at 13:30 UTC. (f) Network-generated MODIS cloud mask without temporal updating at 13:30 UTC.

with the updated CC features has a very close correspondence to the original MODIS cloud mask, whereas the mask created without temporally updated features has clear discrepancies from the original MODIS cloud mask in these regions. The overall classification rates for Fig. 4(d)–(f) are 85.43%, 75.32%, and 65.55%, respectively. Clearly, accounting for the temporal changes in the features aids in the classification of the Meteosat-8 into MODIS-like cloud mask products.

The strong disparity in the correct classification rates for the cloud mask products with and without the temporal updating of the features is illustrated in the confusion matrices in Table III for July 8, 2004, at 13:30 UTC. Again, from the results in this table, it is evident that the mask created by regenerating the mapping matrices is much closer to the original MODIS cloud mask than both the masks created with and without the temporal updating. Note also that the mask generated by regenerating the mapping matrices with new MODIS data tends to overestimate clouds when compared with the masks created without the new MODIS data. In contrast, there is a substantial improvement in the accuracy of cloud estimation in the mask generated with the new MODIS data versus the others, which is evident by comparing the images in Fig. 4(d)–(f). This indicates that the new MODIS data provides a great deal of

TABLE III
CONFUSION MATRICES FOR TEMPORALLY AND NOT TEMPORALLY UPDATED CANONICAL COORDINATE FEATURES OF METEOSAT-8 DATA ON DAY 190 AT 13:30 UTC

		Classification—Regenerated MODIS and Meteosat 8			
		Land		*Water*	
		Cloud	Clear	Cloud	Clear
Original Mask	Cloud	93.32%	6.68%	73.13%	26.87%
	Clear	16.73%	83.77%	7.77%	92.23%
		Classification—Temporally Updated Meteosat 8 only			
		Land		*Water*	
		Cloud	Clear	Cloud	Clear
Original Mask	Cloud	56.47%	43.53%	50.99%	49.01%
	Clear	4.14%	95.86%	2.05%	97.94%
		Classification—Not Temporally Updated			
		Land		*Water*	
		Cloud	Clear	Cloud	Clear
Original Mask	Cloud	48.52%	51.48%	24.45%	75.55%
	Clear	6.00%	94.00%	4.78%	95.22%

TABLE IV
CLOUD MASK RESULTS FOR JULY 7, 2004

MODIS overpass time	% correct w/ temporal update	% correct w/o temporal update
9:45 UTC	92.26%	78.02%
13:00 UTC	83.54%	75.83%
14:30 UTC	84.74%	78.76%

ability to estimate clouds accurately. It is important to notice also that the mask with features that have been temporally updated is significantly better than the mask created without temporal updating, especially in the case of identifying cloudy regions over land. This lends credence to the use of temporal updating for cloud product generation.

To verify the importance of temporal updating of the CC features, the classification scheme is tested on an alternate day. On July 7, 2004, there are three MODIS overpasses within the Meteosat-8 test region. These overpasses occur at 9:45 UTC, 13:00 UTC, and 14:30 UTC. At all of these times, the temporally updated features of Meteosat-8 provide better results than the masks created with features that have not been temporally updated. Table IV gives the measures of the overall classification accuracy for the three overpass times for both with and without the temporal updating of the features. It is clear from this table that the temporally updated CC features of Meteosat-8 give consistently better results in the classification into MODIS-like cloud mask products.

V. CLOUD PHASE PRODUCT GENERATION

The MODIS cloud phase product uses the cloud mask to determine the regions in which clouds are present and then applies another set of tests to determine the composition of those clouds, namely water, ice, or mixed phase. There is also an unknown designation for cases in which the test results are inconclusive. In these tests, only MODIS infrared wavelengths 8.55 and 11.03 μm are utilized for determining the cloud phase. For this paper, clouds are classified as either water phase or ice phase. The mixed and unknown phases are not classified as they are not separable from the ice phase class in the CC feature space. Since the cloud phase product cannot be created without the cloud mask product, only the regions classified as clouds in the MODIS-like cloud mask are used in the analysis of the quality of the cloud phase product generation. This is done for two reasons: 1) prevent errors of the cloud mask generation process to propagate into the cloud phase generation and 2) assess the performance of the cloud phase generation process independent from the cloud mask results.

After the creation of the MODIS-like cloud mask, the regions designated as clouds can be further separated into distinct phases. To do this, several BPNNs are trained to classify the top three infrared CCs of Meteosat-8 SEVIRI into MODIS-like cloud phase products. Each network in the set has the same structure as the ones used for cloud mask generation in Section IV. Again, there are a total of eight networks for generating MODIS-like cloud phase products. A pair of BPNNs is trained for every 2 h during the 8-h daytime period. Each BPNN in a pair is trained separately over land or water based on cloud phase labels from the original MODIS cloud phase product. The input to each BPNN is a 3-D vector consisting of the top three infrared CCs of Meteosat-8. Each BPNN has 12 neurons in the first hidden layer, six neurons in the second hidden layer, and two output neurons corresponding to the ice and water phase classes. A hard-limiting threshold function is performed on the output of each BPNN to yield a cloud phase label.

Training data samples for the cloud phase classification system are randomly drawn from the MODIS cloud phase products from the week of July 7, 2004, through July 15, 2004. A total of 7500 samples are taken for each of the two cloud phase classes. These training samples are utilized in training the networks for 75 epochs for each of the BPNNs. A total of 25 weight initializations are tried for each network, and the network that led to the best performance on the training data was selected for subsequent testing. The selected networks have classification rates between 93% and 96% on the training data. Note that the comparison of the network results and the original MODIS cloud phase products for ice or water phases is made only on a subset of the testing data corresponding to the areas where the network-generated cloud mask classified as clouds.

The results of the cloud phase classification process are substantially better than those for the cloud mask product. Moreover, the phase products created with the temporally updated features have considerably better quality than those that did not use temporally updated features. The original MODIS cloud phase product and the corresponding network-generated cloud phase product at 12:00 UTC on July 8, 2004, are found in Fig. 5(a) and (b), respectively. Notice that there are regions in the network-generated cloud phase product that are classified as clear while they are not clear in the original MODIS phase product. This is due to misclassifications in the cloud mask

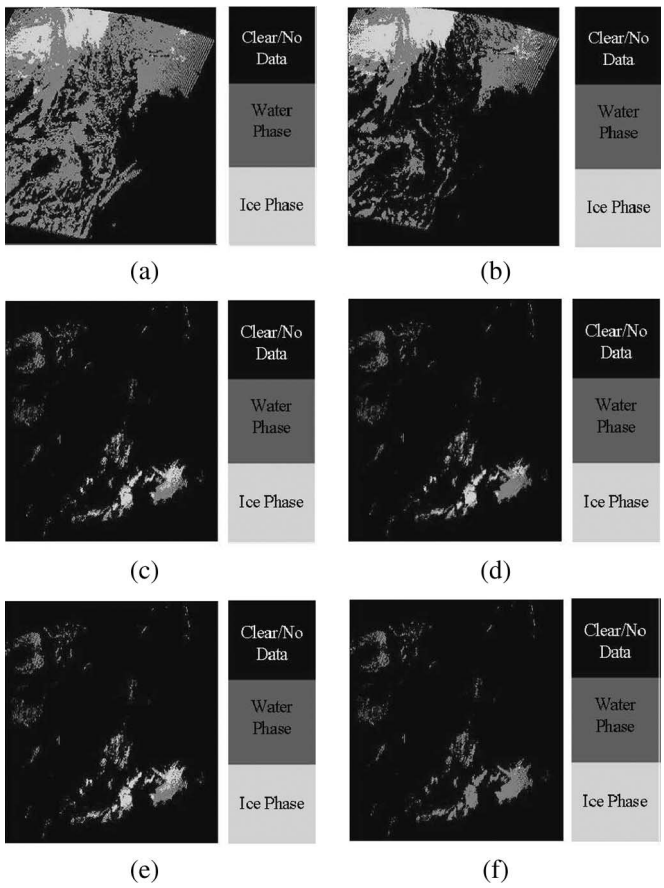

Fig. 5. MODIS cloud phase and network-generated results on July 8, 2004. (a) MODIS cloud phase at 12:00 UTC. (b) Network-generated MODIS cloud phase at 12:00 UTC. (c) MODIS cloud phase at 13:30 UTC. (d) Network-generated cloud phase with retraining using both Meteosat-8 and MODIS at 13:30 UTC. (e) Network-generated cloud phase with temporal updating of only Meteosat-8 at 13:30 UTC. (f) Network-generated MODIS cloud phase without temporal updating at 13:30 UTC.

generation process that are not considered in the analysis of the cloud phase product. The network-generated cloud phase product at 12:00 UTC has an overall accuracy of 93.97%, which indicates that the classification scheme is capable of successfully distinguishing between ice and water phase clouds.

To further illustrate the real usefulness of the temporal updating process, the MODIS cloud phase product on July 8, 2004, at 13:30 UTC is given in Fig. 5(c) as a benchmark. The network-generated cloud phase with the recalculated mapping matrices and using both MODIS and Meteosat-8 is given in Fig. 5(d), while the network-generated cloud phase with only temporally updated Meteosat-8 features (and no new MODIS data) is given in Fig. 5(e). Fig. 5(f), on the other hand, shows the cloud phase product created without any temporal updating of the features. First, we note from Fig. 5(d) and (e) that inclusion of the new MODIS data did not make a significant impact on the cloud phase generation, although ice clouds over water (upper left portion) are better classified. Overall, the correct classification percentages of these images are 91.78% for the phase product in Fig. 5(d) that used data from both satellites and 85.92% for the cloud phase product in Fig. 5(e) that used only temporally updated Meteosat-8 features. Obviously, inclusion of the MODIS data accounts for the statistical changes

TABLE V
CLOUD PHASE CONFUSION MATRICES FOR TEMPORALLY AND NOT TEMPORALLY UPDATED CANONICAL COORDINATE FEATURES FOR JULY 8, 2004 AT 13:30 UTC

		Classification Result - Regenerated MODIS and Meteosat 8			
		Land		*Water*	
		Ice	Water	Ice	Water
Original	Ice	71.46%	28.54%	94.24%	5.76%
Phase	Water	8.68%	91.32%	2.18%	97.82%
		Classification Result - Temporally Updated Meteosat 8 only			
		Land		*Water*	
		Ice	Water	Ice	Water
Original	Ice	72.52%	27.48%	82.15%	17.85%
Phase	Water	10.19%	89.81%	0.80%	99.20%
		Classification Result - Not Temporally Updated			
		Land		*Water*	
		Ice	Water	Ice	Water
Original	Ice	2.96%	97.04%	12.75%	87.25%
Phase	Water	0.07%	99.93%	0.05%	99.95%

that occur in the new MODIS data, resulting in better cloud phase product generation. Perhaps, more important than this comparison is that between the cloud phase products created with and without the temporally updated features in Fig. 5(e) and (f), respectively. Notice that, in the phase product that used no temporal updating of the features, virtually all of the clouds are labeled as water phase clouds, resulting in an overall correct classification rate of only 53.90%, which is clearly unacceptable.

The strong disparity in the correct classification rates of the cloud phase products with or without temporally updating is illustrated in the confusion matrices in Table V for July 8, 2004, at 13:30 UTC. Notice that, in all cases, the correct classification rate of the water phase clouds is approximately 90% or better. However, in the case of ice phase, the product created with temporally updated features has a correct classification rate of 72.52% versus only 2.96% for that without temporally updated features. In comparison, the cloud phase products generated when using both MODIS and Meteosat-8 data are only slightly better than those created with temporally updated features with no new MODIS data.

Finally, to verify the importance of CC updating on the data of other days, tests are performed for cloud phase product development on July 7, 2004. Table VI gives the correct classification rates for the cloud phase products with and without the temporally updated features at each overpass on July 7, 2004. Columns 2–3 in this table correspond to the case where the evaluation area is restricted to only the portion that is correctly classified in the cloud mask generation process, whereas columns 4–5 in this table provide the results over the entire area covered by MODIS and not just the area correctly classified in the cloud mask generation process. Although, in practice,

TABLE VI
CLOUD PHASE PRODUCT RESULTS FOR JULY 7, 2004

MODIS overpass time	% correct w/ temporal update	% correct w/o temporal update	% correct overall w/ temporal update	% correct overall w/o temporal update
9:45 UTC	73.70%	64.13%	72.85%	61.45%
13:00 UTC	95.43%	79.70%	94.32%	77.90%
14:30 UTC	93.29%	62.64%	91.43%	60.66%

only areas correctly classified as clouds would be further classified into phases, these results are given here for the sake of completeness. Clearly in all cases, the temporally updated features give significantly higher quality results. An important note should be made at the 9:45 UTC overpass. At this time, there are very few ice phase pixels, and thus, misclassification of a very small number of pixels can lead to a large drop in overall classification rate. However, at this point, the temporally updated features still outperform the case without any temporal updating. Overall, these results attest to the importance of the temporal updating of Meteosat-8 CC features for generating MODIS-like cloud mask and phase products that are scientifically meaningful and consistent.

VI. BENCHMARKING AND PERFORMANCE ASSESSMENT

In order to assess the performance of our method, a comparison was carried out with an independent Meteosat-8 SEVIRI-based method for generating cloud mask and cloud phase products. This method, which was developed by the Cooperative Institute for Research in the Atmosphere (CIRA) at Colorado State University, is based upon the 8.7-μm IR cloud test using a standard thresholding technique [26], [27] applied against a background brightness temperature database (BBTD). The BBTD is composed of the warmest pixels observed at a given time over a 15-day period. Visual inspection of the Meteosat-8 data confirmed that, virtually, all regions within this data set were cloud free at some time during this 15-day period, thereby greatly enhancing the effectiveness of the applied background threshold cloud test. This test then flags the analysis pixel as cloud-filled when the difference between the BBTD and the current satellite brightness temperature exceeds the value of the defined threshold. A different threshold is used over land and water. The land/water points are identified with a land/water mask. The 8.7-μm thresholds used in these tests are 20 K over land and 5 K over water.

A similar cloud thresholding method is applied to the 0.8-μm Meteosat-8 SEVIRI data. The current satellite reflectance is thresholded against a 15-day background reflectance database (BRD). The BRD consists of the darkest satellite pixel observed at a given time over a 15-day period. The 0.8-μm thresholds used in these tests are 0.25 over land and 0.1 over water. All 0.8-μm Meteosat-8 data used in these cloud tests have been corrected for solar zenith angle dependence.

The original MODIS cloud mask used in this paper is shown again to facilitate the benchmarking in Fig. 6(a) and (b) for July 8, 2004, 12:00 UTC and 13:30 UTC, respectively. The cloud masks obtained using the CIRA Meteosat-8 method are then shown in Fig. 6(c) and (d), covering the same time

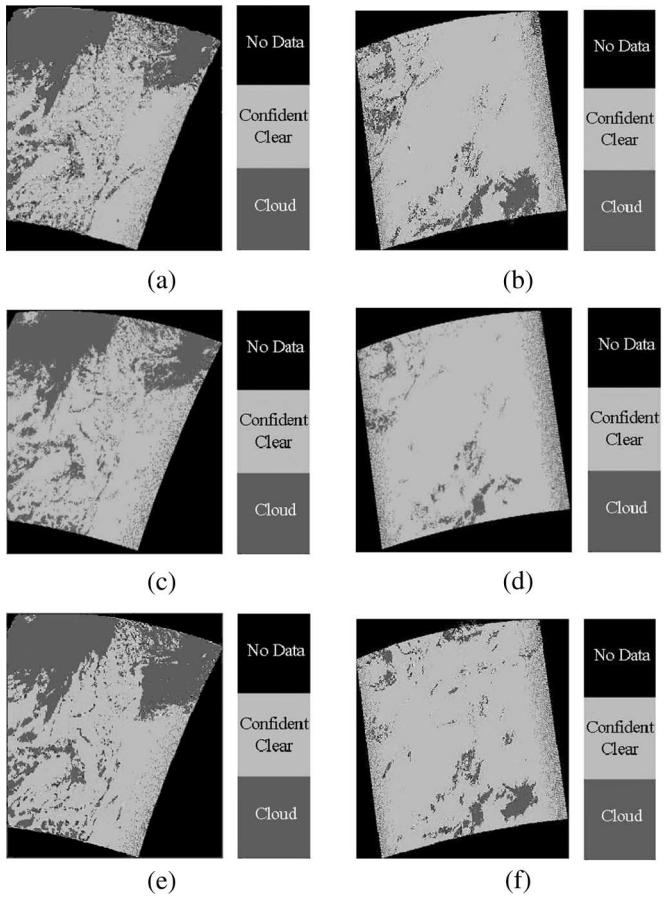

Fig. 6. MODIS cloud mask, CIRA, and networked-generated results on July 8, 2004. (a) MODIS cloud mask at 12:00 UTC. (b) MODIS cloud mask at 13:30 UTC. (c) CIRA cloud mask at 12:00 UTC. (d) CIRA cloud mask at 13:30 UTC. (e) Network-generated MODIS-Like cloud mask at 12:00 UTC. (f) Network-generated MODIS-Like cloud mask using temporal updating of only Meteosat-8 at 13:30 UTC.

frame. The network-generated MODIS-like cloud mask at time 12:00 UTC and that generated with temporal updating of just Meteosat-8 CCs up to and including 13:30 UTC are shown in Fig. 6(e) and (f), respectively. Visual evaluation of these results reveals that the cloud masks generated using our approach are much closer to those of the actual MODIS masks in Fig. 6(a) and (b). This is particularly true for the cloud mask at time 13:30 UTC, where both methods use only the Meteosat-8 data. Nonetheless, the fact that our methods utilize a temporal updating of the CC features over a sequence of Meteosat-8 and MODIS (when available) passes enable these features to capture highly common attributes of the data of both instruments, hence leading to a much better reproduction of MODIS cloud mask. The overall classification rates for the CIRA Meteosat-8

TABLE VII
CONFUSION MATRICES FOR CIRA METHOD AND NETWORK-GENERATED TEMPORALLY UPDATED CLOUD MASK FOR JULY 8, 2004

		Classification Results MODIS-Like cloud mask–12:00 UTC			
		Land		*Water*	
		Cloud	Clear	Cloud	Clear
Original Mask	Cloud	99.77%	0.23%	84.06%	15.94%
	Clear	13.26%	86.74%	5.01%	94.99%

		Classification Results—Temporal Updated w/o MODIS MODIS-Like cloud mask–13:30 UTC			
		Land		*Water*	
		Cloud	Clear	Cloud	Clear
Original Mask	Cloud	56.47%	43.53%	50.99%	49.01%
	Clear	4.14%	95.86%	2.05%	97.94%

		Classification Results CIRA cloud mask–12:00 UTC			
		Land		*Water*	
		Cloud	Clear	Cloud	Clear
Original Mask	Cloud	83.24%	16.76%	78.91%	21.09%
	Clear	2.90%	97.10%	6.80%	93.20%

		Classification Results CIRA cloud mask–13:30 UTC			
		Land		*Water*	
		Cloud	Clear	Cloud	Clear
Original Mask	Cloud	30.95%	69.05%	36.44%	63.56%
	Clear	0.55%	99.45%	1.16%	98.84%

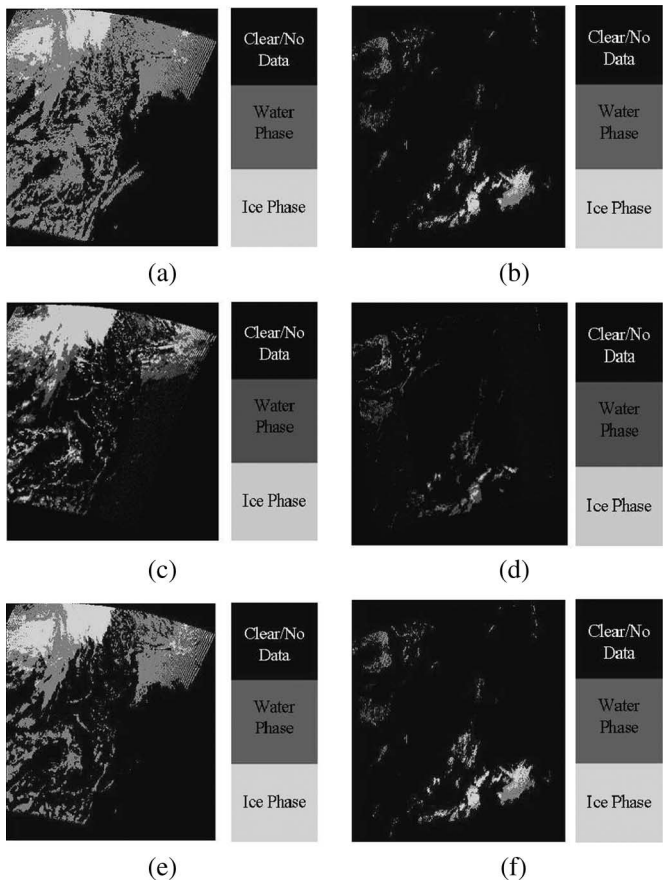

Fig. 7. MODIS cloud phase and CIRA results on July 8, 2004. (a) MODIS cloud phase at 12:00 UTC. (b) MODIS cloud phase at 13:30 UTC. (c) CIRA cloud phase at 12:00 UTC. (d) CIRA cloud phase at 13:30 UTC. (e) Network-generated MODIS cloud phase at 12:00 UTC. (f) Network-generated cloud phase with temporal updating of only Meteosat-8 at 13:30 UTC.

algorithm are found to be 88.56% and 90.83% for 12:00 UTC and 13:30 UTC, respectively, and 91.40% and 85.43% for the same times using our method.

Table VII shows the confusion matrices for CIRA cloud mask and the MODIS-like cloud masks generated using our approach. The percentages in these matrices are obtained based upon the original MODIS cloud masks at times 12:00 UTC and 13:30 UTC as benchmarks. Thus, they show how good the methods can generate a cloud mask similar to MODIS. As can be observed from these results, although the CIRA algorithm provides better results classifying clear pixels, especially over land, it performs rather poorly, capturing the same cloud areas classified by MODIS.

The daytime cloud phase algorithm developed by CIRA starts with the produced cloud mask. If a pixel is cloudy, according to the cloud mask, then the cloud phase algorithm is applied. If it is not cloudy, the algorithm is not applied. The cloud phase algorithm has two parts. First, if the 8.7-μm brightness temperature is less than -30 °C, the pixel is classified as ice cloud. If the pixel is -30 °C or warmer, a second test is applied. This second test relies on three reflective wavelengths, namely 1.6, 0.8, and 0.6 μm. The albedo (reflectance corrected for solar zenith angle) is calculated for each wavelength. The albedo is theoretically between zero and one. The albedos are multiplied by 255 and assigned a color: 1.6 is red (R), 0.8 is green (G), and 0.6 is blue (B). In the resulting image, the ocean is dark because it is poorly reflective at all three wavelengths; vegetated land is green because chlorophyll is reflective at 0.8 μm, but absorptive at 1.6 and 0.6 μm; bare land is brown to red; liquid water clouds are white because they are highly reflective at all three wavelengths; and ice clouds are cyan because they are highly reflective at 0.8 and 0.6 μm, but poorly reflective at 1.6 μm.

For each cloudy pixel (-30 °C or warmer), the R, G, and B values are transformed by one of the several color analysis schemes into, for example, hue (H), saturation (S), and lightness (L). The important parameter is hue (H), which varies in a "color wheel" from 0 (red) to 2/12 (yellow) to 4/12 (green) to 6/12 (cyan) to 8/12 (blue) to 10/12 (magenta) and back to 12/12 (red). The phase algorithm classifies any cloudy pixel with H between 5/12 and 7/12 as ice cloud. All other cloudy pixels are liquid water clouds. This process results in a two-class cloud phase image. Clearly, the algorithm can be fooled by snow on the ground, which is also cyan in color (with these three wavelengths).

The original MODIS cloud phase benchmarks used in this paper are shown in Fig. 7(a) and (b) for July 8, 2004, 12:00 UTC and 13:30 UTC, respectively. The corresponding cloud phase

TABLE VIII
CONFUSION MATRICES FOR CIRA METHOD AND NETWORK-GENERATED TEMPORALLY UPDATED CLOUD PHASE FOR JULY 8, 2004

		Classification Results MODIS-Like phase at 12:00 UTC			
		Land		*Water*	
		Ice	Water	Ice	Water
Original	Ice	85.71%	14.29%	96.38%	3.62%
Phase	Water	0.71%	99.29%	3.24%	96.76%
		Classification Results—Temporal Updated w/o MODIS MODIS-Like phase at 13:30 UTC			
		Land		*Water*	
		Ice	Water	Ice	Water
Original	Ice	72.52%	27.48%	82.15%	17.85%
Phase	Water	10.19%	89.81%	0.80%	99.20%
		Classification Results CIRA cloud phase 12:00 UTC			
		Land		*Water*	
		Ice	Water	Ice	Water
Original	Ice	68.55%	31.45%	91.15%	8.85%
Phase	Water	24.68%	75.32%	46.49%	53.51%
		Classification Results CIRA cloud phase 13:30 UTC			
		Land		*Water*	
		Ice	Water	Ice	Water
Original	Ice	17.37%	82.63%	99.74%	0.26%
Phase	Water	11.04%	88.96%	28.84%	71.16%

products generated using the CIRA method are shown in Fig. 7(c) and (d). The cloud phase products generated using the network with the temporally updated CC features are shown in Fig. 7(e) and (f). Again, visual evaluation of these results shows a much better reproduction of the MODIS cloud phase using our algorithm when compared to CIRAs method. The overall correct classification rates for the CIRA algorithm are 69.05% and 63.66% for 12:00 UTC and 13:30 UTC, respectively, in comparison with 97.16% and 91.84% for our approach.

Table VIII gives the confusion matrices for CIRA cloud phase and our MODIS-like cloud phase at 12:00 UTC and 13:30 UTC. Note that the percentages in these matrices are obtained based upon the match with the actual MODIS cloud phases at these times and over the areas classified as clouds in their respective cloud masks. Clearly, these areas and their sizes in the generated cloud masks are different for the two algorithms. However, since the numbers of pixels in these areas are large, the percentages are representative of the ensemble statistics. Owing to the fact that CIRAs algorithm is not designed to mimic what MODIS produces, the percentages are vastly different, especially at 13:30 UTC. This is due to the fact that, at 13:30 UTC, the discrepancy between MODIS cloud mask and CIRA-generated could mask is substantial.

Overall, it is evident from the results presented in this section that, when MODIS is used as the benchmark, the cloud products generated using our neural network with temporally updated CC features are significantly better than those of the CIRA method, which uses only the Meteosat-8 data.

VII. OBSERVATIONS AND CONCLUSION

A temporally adaptive method for creating features of an operational satellite that are most coherent with a scientific research satellite is introduced in this paper. The extracted features capture highly coherence attributes between the two satellites, allowing for the creation of cloud products that are research-quality, especially at times and locations that the MODIS data are unavailable. These products are generated without using any cloud physical models or auxiliary information typically needed by the conventional methods. The proposed method provides a means of creating research-quality products not only with temporal consistency but also with spatial spreading. Moreover, the temporal updating mechanism enables continual generation of cloud products during the daytime when only the operational satellite provides new data. Land and water features are separated to allow for distinction between the statistical features of these two classes. In the case of both the cloud mask and the cloud phase, the results indicated that the temporally updated features provide much better cloud classification than those without temporal updating. Specifically, the cloud masks generated with temporally updated features provide better identification of cloudy regions than those without temporally updated features. Additionally, the cloud phase generation process with the temporally updated features gave much better ice phase cloud determination when compared to the case without updated features. Overall, the temporal updating process allows for the incorporation of the statistical changes in the new data while retaining the information in the previous data, hence resulting in better cloud mask/phase products.

The results in this paper show the great promise of the proposed CCD-based feature extraction method, together with a mechanism for temporal updating of the CC features for dual-satellite data analysis. Other potential remote-sensing applications of the proposed method include aerosol and fire detection, ocean thermal monitoring, etc.

ACKNOWLEDGMENT

The authors would like to thank J. D. Tucker from the ECE Department for the help and S. Kidder at CIRA, Colorado State University, for carrying out the benchmarking studies with CIRAs algorithm.

REFERENCES

[1] G. S. Pankiewicz, "Pattern recognition techniques for identification of cloud and cloud systems," *Meteorol. Appl.*, vol. 2, pp. 257–271, Sep. 1995.
[2] P. M. Tag, R. L. Bankert, and L. R. Brody, "An AVHRR multiple cloud-type classification package," *J. Appl. Meteorol.*, vol. 39, no. 2, pp. 125–134, Feb. 2000.
[3] R. L. Bankert, M. Hadjimichael, A. P. Kuciauskas, K. L. Richardson, J. Turk, and J. D. Hawkins, "Automating the estimation of various

meteorological parameters using satellite data and machine learning techniques," in *Proc. IEEE Int. Geosci. and Remote Sens. Symp.*, 2002, pp. 708–710.
[4] D. W. Reynolds and T. H. Vonder Haar, "Bi-spectral method for cloud parameter determination," *Mon. Weather Rev.*, vol. 105, no. 4, pp. 446–457, Mar. 1977.
[5] R. M. Welch, K. S. Kuo, S. K. Sengupta, and D. W. Chen, "Cloud field classification based on high spatial resolution textural feature (I): Gray-level cooccurrence matrix approach," *J. Geophys. Res.*, vol. 93, no. D10, pp. 12 663–12 681, Oct. 1988.
[6] D. W. Chen, S. K. Sengupta, and R. M. Welch, "Cloud field classification based on high spatial resolution textural feature (II): Simplified vector approaches," *J. Geophys. Res.*, vol. 94, no. D12, pp. 14 749–14 765, Oct. 1989.
[7] B. Tian, M. A. Shaikh, M. R. Azimi-Sadjadi, and T. H. Vonder Haar, "A study of cloud classification with neural networks using spectral and textural features," *IEEE Trans. Neural Netw.*, vol. 10, no. 1, pp. 138–151, Jan. 1999.
[8] B. Tian, M. R. Azimi-Sadjadi, T. H. Vonder Haar, and D. Reinke, "Temporal updating scheme for probabilistic neural network with application to satellite cloud classification," *IEEE Trans. Neural Netw.*, vol. 11, no. 4, pp. 903–920, Jul. 2000.
[9] J. Wang and M. R. Azimi-Sadjadi, "A temporally adaptive classifier for multispectral imagery," *IEEE Trans. Neural Netw.*, vol. 15, no. 1, pp. 159–165, Jan. 2004.
[10] J. C. B. Melo, G. D. C. Cavalcanti, and K. S. Guimardes, "PCA feature extraction for protein structure prediction," in *Proc. IEEE Int. Joint Conf. Neural Netw.*, 2003, pp. 2952–2957.
[11] K. S. Huang and M. M. Trivedi, "Streaming face recognition using multicamera video arrays," in *Proc. IEEE Int. Conf. Pattern Recog.*, 2002, pp. 213–216.
[12] E. Maeda, H. Tanaka, A. Shio, and K. Ishii, "Robust object extraction using normalized principal component features," in *Proc. IEEE Conf. Image, Speech, and Signal Anal.*, 1992, pp. 151–155.
[13] A. J. Bell and T. J. Sejnowski, "The 'independent components' of natural scenes are edge filters," *Vis. Res.*, vol. 37, no. 23, pp. 3327–3338, Dec. 1997.
[14] J. Hurri, A. Hyvärinen, and E. Oja, "Wavelets and natural image statistics," in *Proc. Scand. Conf. Image Anal.*, 1997, pp. 13–18.
[15] I. R. Farah, M. B. Ahmed, M. S. Naceur, and M. R. Boussema, "Satellite image analysis based on the method of blind separation of sources for the extraction of information," in *Proc. IEEE Geosci. and Remote Sens. Symp.*, 2002, pp. 919–921.
[16] H. Okumura, T. Sugita, H. Matsumoto, and N. Takeuchi, "Noise reduction method for lidar echo data based on multivariate analysis method," in *Proc. IEEE Int. Geosci. and Remote Sens. Symp.*, 1993, pp. 454–456.
[17] E. D. Hernandez-Baquero and J. R. Schott, "Atmospheric and surface parameter retrievals from multispectral thermal imagery via reduced-rank multivariate regression," in *Proc. IEEE Int. Geosci. and Remote Sens. Symp.*, 2000, pp. 1525–1527.
[18] G. Lui, S. Dong, and H. Peng, "Research on land use/cover change of hilly and gully area in the Loess Plateau," in *Proc. IEEE Int. Geosci. and Remote Sens. Symp.*, 2004, pp. 3436–3439.
[19] E. LeDrew, C. Derksen, and B. Goodison, "Determination of the dominant spatial modes of terrestrial snow cover over North America using passive microwave derived data," in *Proc. IEEE Int. Geosci. and Remote Sens. Symp.*, 1997, pp. 1672–1674.
[20] I. Niemeyer and M. Canty, "Possibilities and limits of remote sensing for the verification of international agreements: Algorithms to detect changes at nuclear plants," in *Proc. IEEE Int. Geosci. and Remote Sens. Symp.*, 1998, pp. 819–821.
[21] I. Niemeyer, M. Canty, and D. Klaus, "Unsupervised change detection techniques using multispectral satellite images," in *Proc. IEEE Int. Geosci. and Remote Sens. Symp.*, 1999, pp. 327–329.
[22] R. Lindsey and D. Herring, "MODIS (Moderate Resolution Imaging Spectroradiometer)," *NASA Bulletins*, 2002, Greenbelt, MD: Goddard Space Flight Center.
[23] S. Ackerman, K. Strabala, P. Menzel, R. Frey, C. Moeller, L. Gumley, B. Baum, S. W. Seeman, and H. Zhang, *Discriminating Clear-Sky From Cloud With MODIS—NASA Algorithm Theoretical Basis Document (MOD35)*. Greenbelt MD: NASA 2002.
[24] W. P. Menzel, B. A. Baum, K. I. Strabala, and R. A. Frey, *Cloud Top Properties and Cloud Phase—NASA Algorithm Theoretical Basis Document*, 6th ed. Greenbelt, MD: NASA, 2002.
[25] J. Schmetz, P. Pili, S. Tjemkes, D. Just, J. Kerkmann, S. Rota, and A. Ratier, "An introduction to Meteosat second generation (MSG)," *Bull. Amer. Meteorol. Soc.*, vol. 83, no. 7, pp. 977–992, Jul. 2002.
[26] D. L. Reinke, C. L. Combs, S. Q. Kidder, and T. H. Vonder-Haar, "Satellite cloud composite climatologies: A new high resolution tool in atmospheric research and forecasting," *Bull. Amer. Meteorol. Soc.*, vol. 73, no. 3, pp. 278–285, 1992.
[27] R. A. Schiffer and W. B. Rossow, "The International Satellite Cloud Climatology Project (ISCCP): The first project of the world climate research programme," *Bull. Amer. Meteorol. Soc.*, vol. 64, no. 7, pp. 779–784, 1983.
[28] L. L. Scharf and C. T. Mullis, "Canonical coordinates and the geometry of inference, rate, and capacity," *IEEE Trans. Signal Process.*, vol. 48, no. 3, pp. 824–831, Mar. 2000.
[29] C. E. Shannon, "A mathematical theory of communication," *Bell Syst. Tech. J.*, vol. 27, pp. 379–423, Jul.–Oct. 1948. 623-656.
[30] A. Pezeshki, L. L. Scharf, M. R. Azimi-Sadjadi, and Y. Hua, "Two-channel constrained least squares problems: Solutions using power methods and connections with canonical coordinates," *IEEE Trans. Signal Process.*, vol. 53, no. 1, pp. 121–135, Jan. 2005.
[31] G. H. Golub and C. F. Van Loan, *Matrix Computations*, 3rd ed. Baltimore, MD: The Johns Hopkins Univ. Press, 1996.
[32] S. Haykin, *Neural Networks, A Comprehensive Foundation*, 2nd ed. Englewood Cliffs, NJ: Prentice-Hall, 1999.

Amanda K. Falcone received the B.S. degree in engineering science (*with honors*), with specialization in electrical engineering, from Trinity University, San Antonio, TX, in 2003, and the M.S. degree in electrical engineering from Colorado State University, Fort Collins, in 2005.

She is currently employed as an Engineer with the Northrop Grumman, Aurora, CO, performing algorithm development. Her main research interests include signal/image processing, estimation and Kalman filtering theory, and applications of neural networks.

Mahmood R. Azimi-Sadjadi (S'81–M'81–SM'89) received the M.S. and Ph.D. degrees from Imperial College of Science and Technology, University of London, London, U.K., in 1978 and 1982, respectively, all in electrical engineering, with specialization in digital signal/image processing.

He is currently a Full Professor with the Electrical and Computer Engineering Department, Colorado State University (CSU), Fort Collins. He is also the Director of the Digital Signal/Image Laboratory, CSU. His main areas of interest include digital signal and image processing, wireless sensor networks, target detection, classification and tracking, adaptive filtering, system identification, and neural networks. His research efforts in these areas resulted in over 250 journals and referenced conference publications. He is the coauthor of the book *Digital Filtering in One and Two Dimensions* (Plenum Press, 1989).

Prof. Azimi-Sadjadi is the recipient of the 1999 ABEL Teaching Award, 1993 ASEE-Navy Senior Faculty Fellowship Award, 1991 CSU Dean's Council Award, and 1984 DOW Chemical Outstanding Young Faculty Award. He has served as an Associate Editor of the IEEE TRANSACTIONS ON SIGNAL PROCESSING and the IEEE TRANSACTIONS ON NEURAL NETWORKS.

J. Adam Kankiewicz received the B.S. degree (*summa cum laude*) from the University of California, Los Angeles, in 1998, and the M.S. degree from Colorado State University, Fort Collins, in 1995, all in atmospheric science.

He is currently a Research Associate III with the Cooperative Institute for Research in the Atmosphere (CIRA), Colorado State University. His research interests include radar remote-sensing techniques, analyzing visible and infrared satellite data, and analyzing cloud microphysical data. As a Project Manager for CIRA's Cloud Layer Experiment program, he coordinates field campaign studies of mid-level mixed-phase clouds. He also coordinates geostationary satellite data deliveries to the International Satellite Cloud Climatology Project.